Solutions of complete jump relations at discontinuities in a two-and-half-dimensional reconnection model

Marina Skender,[1,*] Bojan Vršnak,[2,†] and Mladen Martinis[1,‡]

[1]*Rudjer Bošković Institute, Bijenička 54, HR-10000 Zagreb, Croatia*
[2]*Hvar Observatory, Faculty of Geodesy, Kačićeva 26, HR-10000 Zagreb, Croatia*

We present an analytic solution of the complete set of jump relations at the rotational discontinuity and the slow-mode shock in a two-and-half-dimensional ($2\frac{1}{2}$D) symmetric reconnection model. The solution is used for analyzing the outflow jet characteristics in dependence on the speed and the incidence angle of the inflowing plasma, for a given shear of the inflow magnetic field. It is found that the magnetosonic Mach number of the outflow depends significantly on the incidence angle, the effect being more prominent at larger reconnection rates. The compression increases weakly with increasing reconnection rate. Dynamical changes in the flow/field geometry are found in the transition to the 2D regime: In the region between the rotational discontinuity and the slow-mode shock the direction of flow and the magnetic field become extremely sensitive to the degree of the magnetic field shear in the inflow. Implications for evolutionary systems such as solar flares are discussed.

PACS number(s): 52.35.Tc

I. INTRODUCTION

When two highly conductive plasma systems with oppositely directed magnetic fields merge, the electric current sheet is created in between [1]. Such systems often become unstable, abruptly releasing the magnetic field energy in the form of intense heating, violent plasma flows, and particle acceleration. Explosive energy release of this kind is observed in solar and stellar flares, in magnetospheres of planets and comets, as well as in laboratory phenomena (cf. Refs. [1,2], and references therein).

The current sheet becomes unstable when its length-to-width ratio surpasses the tearing instability threshold [3,4]. The instability results in fast reconnection of magnetic field lines, which makes possible high-energy release rate. The field lines reconnect within a tiny diffusion region whose dimensions are much smaller than the overall scale of the system. The reconnected field lines are strongly bent, and the magnetic field tension accelerates the plasma to form two jets of outflowing plasma. Plasma convected out of the diffusion region is replaced by new plasma drawn from the external region, which also brings in a "fresh" magnetic field to be reconnected. In the fast reconnection regime the Mach Alfvén number of the inflow can be up to $M_A \approx 0.1$ [1].

The inflowing plasma moves almost perpendicularly to the magnetic field, so the plasma flow is faster than the corresponding slow-mode magnetoacoustic speed. Consequently, two pairs of slow-mode standing (SMS) shocks appear in the flow "collision," outlining the border between the inflow and the outflow region. In SMSs plasma is heated and compressed, whereas the flow is deflected and accelerated. Such a two-dimensional (2D) model of fast reconnection was proposed by Petschek to explain the powerful energy release in solar flares [5].

Subsequently, Petschek and Thorne extended the model by including two pairs of rotational discontinuities (RDs) in front of SMSs (see Fig. 1) in order to overcome shortcomings inherent to the original 2D model (for details, see Ref. [6]). The inclusion of the RDs enables the application of the model to the situation which includes the transversal magnetic field component B_z perpendicular to the reconnection plane (Fig. 1). All the quantities are taken to be independent of the z coordinate (so-called $2\frac{1}{2}$D reconnection model). The $2\frac{1}{2}$D model inevitably requires a rotation of the outflow tangential component of the magnetic field, which cannot happen at SMS [1]. The tangential component of the magnetic field is rotated at RD, which implies that velocity upstream of the SMS has the z component, v_z (Fig. 1). The density, gas pressure, and magnetic field strength do not change across RDs [1]—the plasma is heated and compressed only at SMSs, such as in the 2D case. In the limit of $B_z \to 0$, RDs merge with SMSs [6].

The 2D reconnection problem was put on a firm mathematical foundation by Soward and Priest [7]. In the subsequent paper Soward extended the consideration to the $2\frac{1}{2}$D case [8]. Yet, the jump conditions at the RD/SMS discontinuity system were greatly simplified by assuming that plasma inflows into the current sheet perpendicularly to the symmetry axis of the system and that the inflow is very slow. This is often violated in astrophysical phenomena, and it is of interest for a wide range of problems to investigate the characteristics of the reconnection system including a non-perpendicular and a relatively fast inflow [9]. Furthermore, it is approximated in Soward's paper that in the region between RD and SMS the transversal magnetic field component is much larger than the tangential one [8]. For this reason, the behavior of the system in the transition from the $2\frac{1}{2}$D to the 2D regime cannot be followed, which could be essential for

---

*Email address: marina@rudjer.irb.hr
†Email address: bvrsnak@geodet.geof.hr
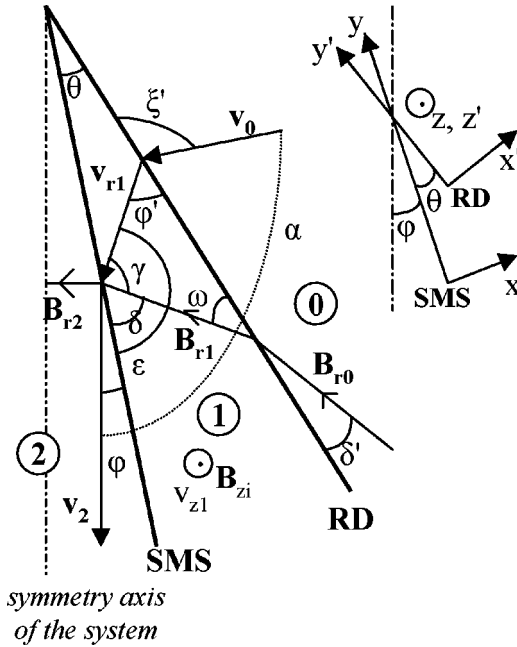‡Email address: martinis@rudjer.irb.hr

68 046405-1

FIG. 1. The geometry of the system of discontinuities in the $2\frac{1}{2}$D symmetrical reconnection problem, depicted in one quadrant. The slow-mode shock (SMS) is inclined to the symmetry axis (dash-dotted line) at the angle ϕ. The angle between the rotational discontinuity (RD) and the SMS is denoted as ϑ. The quantities in the inflow, intermediate, and outflow regions are designated by subscripts "0," "1," and "2," respectively. The xy-plane components of the magnetic field $\vec{B}$ and the flow velocity $\vec{v}$ are denoted by the subscript "r." The direction of the z component of $\vec{B}$ and $\vec{v}$ is also indicated. The incidence angle of the inflow is denoted as α. The y' axis of the "primed" frame of reference is aligned with the RD, while the y axis of the "nonprimed" coordinate system lies aligned with the SMS, as shown upper right.

understanding some aspects of evolutionary systems, such as solar flares [10,11]. It should be emphasized that although the reconnecting magnetic field structures form three-dimensional configurations in reality [1,2,12], a wide range of phenomena could be well described in the 2D or $2\frac{1}{2}$D geometry [10,13].

In this paper we develop an analytical solution of the full set of magnetohydrodynamics (MHD) equations, analytically describing the RD/SMS discontinuity system of the symmetrical $2\frac{1}{2}$D reconnection problem. The solutions are used for analyzing the conditions in the current sheet as a function of the inflow speed and the inflow incidence angle, at a given shear of the magnetic field and the plasma-to-magnetic pressure ratio in the inflow. The mathematical problem is described in Sec. II and the results are presented in Sec. III. The implications and possible applications to solar flares are discussed in Sec. IV.

II. MODEL

A. Description of the system of discontinuities

The system of discontinuities separating the outflow from the inflow region is schematically drawn in Fig. 1, where the

quantities used in the following consideration are defined. The inflow region is marked by "0," the region between RD and SMS by "1," and the outflow region by "2." The xyz-coordinate system, with the y axis aligned to SMS, is inclined at the angle ϕ to the symmetry axis of the system, which is defined by the outflow direction $\vec{v}_2$. The angle between RD and SMS is ϑ, so the $x'y'z'$-coordinate system, with the y' axis aligned to RD, is inclined at the angle $\phi + \vartheta$ to the symmetry axis. The z and z' axes are pointing out of the plane of the figure. The vector components parallel and perpendicular to the symmetry axis of the system (dash-dotted line in Fig. 1) are denoted by indices "$\parallel$" and "$\perp$," respectively ($v_\parallel$, $v_\perp$, $B_\parallel$, $B_\perp$).

In region 0, plasma of the density ρ_0 and the pressure p_0 flows into RD with the velocity $\vec{v}_0$, carrying the magnetic field $\vec{B}_0$. In the intermediate and the outflow region these quantities are denoted by subscripts 1 and 2, respectively. The magnetic field generally has x, y, and z components in all three regions, as does the velocity in region 1, while the velocities in regions 0 and 2 have only the xy-plane components. The magnetic field $\vec{B}_2$ is perpendicular to the velocity $\vec{v}_2$.

B. Jump relations at discontinuities

The jump relations across RD, written out in terms of vector components in the $x'y'z'$-coordinate system (Fig. 1), for the ratio of specific heats $\gamma = \frac{5}{3}$, read [1]

$$B'_{x0} = B'_{x1}, \tag{1}$$

$$\rho_0 v'_{x0} = \rho_1 v'_{x1}, \tag{2}$$

$$B'_{y0} v'_{x0} - B'_{x0} v'_{y0} = B'_{y1} v'_{x1} - B'_{x1} v'_{y1}, \tag{3}$$

$$B'_{x0} v_{z0} - B_{z0} v'_{x0} = B'_{x1} v_{z1} - B_{z1} v'_{x1}, \tag{4}$$

$$p_0 + \frac{B_0^2}{2\mu} - \frac{B'^2_{x0}}{\mu} + \rho_0 v'^2_{x0} = p_1 + \frac{B_1^2}{2\mu} - \frac{B'^2_{x1}}{\mu} + \rho_1 v'^2_{x1}, \tag{5}$$

$$\rho_0 v'_{x0} v'_{y0} - \frac{B'_{x0} B'_{y0}}{\mu} = \rho_1 v'_{x1} v'_{y1} - \frac{B'_{x1} B'_{y1}}{\mu}, \tag{6}$$

$$\rho_0 v'_{x0} v_{z0} - \frac{B'_{x0} B_{z0}}{\mu} = \rho_1 v'_{x1} v_{z1} - \frac{B'_{x1} B_{z1}}{\mu}, \tag{7}$$

$$\left[5p_0 + \rho_0 v_0^2 + \frac{2}{\mu}(B'^2_{y0} + B^2_{z0}) \right] v'_{x0} - \frac{2B'_{x0}}{\mu}(B_{z0} v_{z0} + B'_{y0} v'_{y0})$$

$$= \left[5p_1 + \rho_1 v_1^2 + \frac{2}{\mu}(B'^2_{y1} + B^2_{z1}) \right] v'_{x1} - \frac{2B'_{x1}}{\mu}$$

$$\times (B_{z1} v_{z1} + B'_{y1} v'_{y1}). \tag{8}$$

The jump relations at SMS, written out in terms of vector components in the xyz-coordinate system, form an analogous set of equations: In Eqs. (6)–(13) primes should be

omitted from the x' and y' components, whereas the indices 1 should be replaced by 2, and 0 by 1.

If smaller terms are neglected like in Ref. [8], the system becomes decoupled, so the outflow speed, density, pressure, and magnetic field depend only on the inflow plasma-to-magnetic pressure ratio β_0 and the relative strength of the transversal magnetic field, B_{z0}/B_0, but they do not depend on the inflow speed. This approximation will further on be referred to as the Soward regime.

C. Parametrizing the system

The components of the velocity and the magnetic field in the inflow and the intermediate region are related to the angles defined in Fig. 1 as follows:

$$v'_{x0}=-v_0\sin \xi', \quad v'_{y0}=-v_0\cos \xi',$$

$$v'_{x1}=-v_{r1}\sin \phi', \quad v'_{y1}=-v_{r1}\cos \phi', \quad v'_{z1}=v_1\sin \Omega_V,$$

$$B'_{x0}=-B_{r0}\sin \delta', \quad B'_{y0}=B_{r0}\cos \delta', \quad B'_{z0}=-B_0\sin \Omega_0,$$

$$B'_{x1}=-B_{r1}\sin \omega, \quad B'_{y1}=B_{r1}\cos \omega, \quad B'_{z1}=B_1\sin \Omega_1.$$

The angles Ω_0, Ω_1, and Ω_2 define the ratio of the transversal and the xy-plane component of the magnetic field, $\tan \Omega_i = B_{zi}/B_{ri}$, $i=0,1,2$, whereas Ω_V defines the analogous ratio for the flow velocity in the intermediate region.

At RD the density, gas pressure, the magnetic field strength, and consequently, the temperature and the plasma-to-magnetic pressure ratio, are continuous [8], i.e., $\rho_0=\rho_1$,

$p_0=p_1$, $|B_0|=|B_1|$, $T_0=T_1$, and $\beta_0=\beta_1$, respectively. After applying these additional conditions, it is straightforward to show that two of the jump equations at RD are linearly dependent on other equations. We eliminate Eqs. (10) and (13) as linearly dependent on others and normalize the remaining equations by introducing suitable dimensionless variables $B'_r=B_{r1}/B_{r0}$, $V'_r=v_{r1}/v_0$, $\beta_0=2\mu p_0/B_0^2$, and the xy-plane Mach-Alfvén number in the intermediate region $M_{A1r}=\sqrt{v_{r1}^2\mu\rho_1/B_{r1}^2}$. Equations (6)–(9) yield, respectively,

$$B'_r=\frac{\sin \delta'}{\sin \omega}, \tag{9}$$

$$V'_r=\frac{\sin \xi'}{\sin \phi'}, \tag{10}$$

$$\cot \delta' + \cot \xi' = \cot \omega + \cot \phi', \tag{11}$$

$$\sin \varepsilon' \tan \Omega_0 = -V'_r B'_r \sin \omega \tan \Omega_V + V'_r B'_r \sin \phi' \tan \Omega_1. \tag{12}$$

Combination of Eqs. (6), (8), and (11) reveals that $v'_{x1}\sqrt{\mu\rho_1}/B'_{x1}\equiv M'_{Ax1}=1$, of which the consequence is

$$M_{A1r}=\frac{\sin \omega}{\sin \phi'}. \tag{13}$$

Equations (11) and (12) yield

$$\sin \delta' - B'^2_r\cot \Omega_0\sin \omega \tan \Omega_1 = -\frac{V'^2_r\cos^2\Omega_0(B'^2_r\sin \omega \cos \omega-\sin \delta'\cos \delta')\sin \phi' \tan \Omega_V}{(\sin \xi'\cos\xi' - V'^2_r\sin \phi'\cos \phi')\cos \Omega_0\sin \Omega_0}. \tag{14}$$

The components of the velocity and the magnetic field in the frame of reference aligned with the SMS shock front can be expressed using the angles defined in Fig. 1:

$$v_{x1}=-v_{r1}\sin \varepsilon, \quad v_{y1}=v_{r1}\cos \varepsilon, \quad v_{z1}=v_1\sin \Omega_V,$$

$$v_{x2}=-v_2\sin \phi, \quad v_{y2}=-v_2\cos \phi,$$

$$B_{x1}=-B_{r1}\sin \delta, \quad B_{y1}=B_{r1}\cos \delta, \quad B_{z1}=B_1\sin \Omega_1,$$

$$B_{x2}=-B_{r2}\cos \phi, \quad B_{y2}=B_{r2}\cos \phi, \quad B_{z2}=B_2\sin \Omega_2.$$

Here the dimensionless variables are $B_r=B_{r2}/B_{r1}$, $V_r=v_2/v_{r1}$, $N=\rho_2/\rho_1$, $P=p_2/p_1$, $\beta_{1r}=2\mu p_1/B_{1r}^2$, and $M_{A1r}^2=\mu v_{r1}^2\rho_1/B_{r1}^2$. In region 1, the plasma-to-magnetic pressure ratio is related to β_{1r} as $\beta_1=\beta_{1r}\cos^2\Omega_1$, and the Mach-Alfvén number is $M_{A1}=M_{A1r}\cos \Omega_1/\cos \Omega_V$. The set of jump relations at SMS discontinuity analogous to Eqs. (6)–(13) yields, respectively,

$$B_r=\frac{\sin \delta}{\cos \phi}, \tag{15}$$

$$NV_r=\frac{\sin \varepsilon}{\sin \phi}, \tag{16}$$

$$V_r B_r=\sin \gamma, \tag{17}$$

$$\tan \Omega_1\sin \varepsilon - \tan \Omega_V\sin \delta= V_r B_r\tan \Omega_2\sin \phi, \tag{18}$$

$$\beta_{1r}(1-P)+2M_{A1r}^2(\sin^2\varepsilon - NV_r^2\sin^2 \phi)$$
$$+\frac{1}{\cos^2\Omega_1}-\frac{B_r^2}{\cos^2\Omega_2}=0, \tag{19}$$

$$M_{A1r}^2=\frac{\sin \delta \cos \delta - B_r^2\sin \phi \cos \phi}{\sin \varepsilon \cos\varepsilon + NV_r^2\sin \phi \cos \phi}, \tag{20}$$

$$\tan \Omega_1 \sin \delta = M_{A1r}^2 \tan \Omega_V \sin \varepsilon + B_r^2 \tan \Omega_2 \cos \phi, \quad (21)$$

$$-\frac{5}{4}\beta_{1r}(\sin \varepsilon - PV_r \sin \phi) + F = 0, \quad (22)$$

where the quantity F is to be found in the Appendix.

The angles γ, ω, ϑ, ε, δ, and ϕ' are mutually related (Fig. 1) providing three additional equations:

$$\gamma = \varepsilon - \delta, \quad (23)$$

$$\omega = \pi - \phi' - \gamma, \quad (24)$$

$$\vartheta = \delta - \omega. \quad (25)$$

So the system of discontinuities sketched in Fig. 1 is described by the set of 17 equations from (14) to (30), involving 21 quantities: ξ', ε, N, δ, ϕ, γ, ω, ϑ, ϕ', δ', Ω_0, Ω_1, Ω_V, Ω_2, V_r, B_r, V_r', B_r', M_{A1r}, β_{1r}, and P. We are free to choose four quantities to serve as input parameters. There are several choices which provide solutions in an explicit form. Unfortunately, the system cannot be solved explicitly by taking the inflow quantities as input parameters. The system also turned out to be extremely sensitive to some quantities, entangling numerical evaluations. We have found the most suitable choice of input parameters to be ξ', ε, N, and δ, and for this choice we present an explicit solution of the system.

D. The explicit solution

With the choice of ξ', ε, N, and δ as input parameters, the angle γ is evaluated straightforwardly from Eq. (28), while ϕ, V_r, and B_r are derived from Eqs. (20)–(22):

$$\phi = \frac{1}{2} \arcsin \frac{2 \sin \varepsilon \sin \delta}{N \sin \gamma}, \quad (26)$$

$$V_r = \frac{\cos \phi \sin \gamma}{\sin \delta}, \quad (27)$$

$$B_r = \frac{\sin \delta}{\cos \phi}, \quad (28)$$

providing the evaluation of M_{A1r} from Eq. (25),

$$M_{A1r} = \sqrt{\frac{\sin \delta \cos \delta - B_r^2 \sin \phi \cos \phi}{\sin \varepsilon \cos \varepsilon + N V_r^2 \sin \phi \cos \phi}}. \quad (29)$$

Once M_{A1r} is known, ϕ' is found utilizing Eqs. (18) and (29):

$$\phi' = \arctan \frac{\sin \gamma}{M_{A1r} - \cos \gamma}. \quad (30)$$

From Eqs. (29) and (30) we derive ω and ϑ straightforwardly, and Eq. (16) gives us

$$\delta' = \arctan \frac{1}{\cot \omega + \cot \phi' - \cot \xi'}. \quad (31)$$

The quantities B_r' and V_r' can now be evaluated from Eqs. (14) and (15), respectively. We calculate Ω_V, Ω_0, Ω_1, and Ω_2 combining Eqs. (14), (15), (17), (19), (23), and (26):

$$\Omega_V = \arctan \sqrt{\frac{H^2 - 1}{D^2 - G^2 H^2}}, \quad (32)$$

$$\Omega_0 = \arctan(G \tan \Omega_V), \quad (33)$$

$$\Omega_1 = \arctan(D \tan \Omega_V), \quad (34)$$

$$\Omega_2 = \arctan \frac{\tan \Omega_1 \sin \varepsilon - \tan \Omega_V \sin \delta}{V_r B_r \sin \phi}, \quad (35)$$

where the quantities H, D, and G are written out in the Appendix. Finally, Eqs. (24) and (27) give

$$P = \frac{\dfrac{4F}{5E} + \sin \varepsilon}{V_r \sin \phi + \dfrac{4F}{5E}}, \quad (36)$$

$$\beta_{1r} = -\frac{E}{1 - P}, \quad (37)$$

where E and F are to be found in the Appendix. For the chosen input parameters ξ', ε, N, and δ, Eqs. (28)–(42) together with Eqs. (14) and (15) are the explicit solution of the $2\frac{1}{2}$D reconnection problem.

The inflow Mach-Alfvén number $M_{A0} = v_0/v_{A0}$, where $v_{A0} = B_0/\sqrt{\mu \rho_0}$ is the Alfvén speed of the inflowing plasma, becomes

$$M_{A0} = \sqrt{\frac{B_r'^2 \sin \omega \cos \omega - \sin \delta' \cos \delta'}{\sin \xi' \cos \xi' - V_r'^2 \sin \phi' \cos \phi'}} \cos \Omega_0. \quad (38)$$

The quantity of particular interest is the ratio of the inflow velocity component perpendicular to the symmetry axis of the system and the Alfvén speed based on the component of the magnetic field parallel to the symmetry axis $M_{A00} = v_{0\perp}/v_{A0\parallel} = v_{0\perp}\sqrt{\mu \rho_0}/B_{0\parallel}$, representing the dimensionless reconnection rate [1]. Inspecting Fig. 1 and utilizing $M_{Ax1}' = 1$ one finds

$$M_{A00} = \frac{\sin \alpha \sin \delta'}{\sin(\pi - \xi')\cos(\delta' + \vartheta + \phi)}. \quad (39)$$

The plasma-to-magnetic pressure ratio in the inflow region β_0 is related to β_{1r} as

$$\beta_0 = \beta_1 = \beta_{1r} \cos^2 \Omega_1. \quad (40)$$

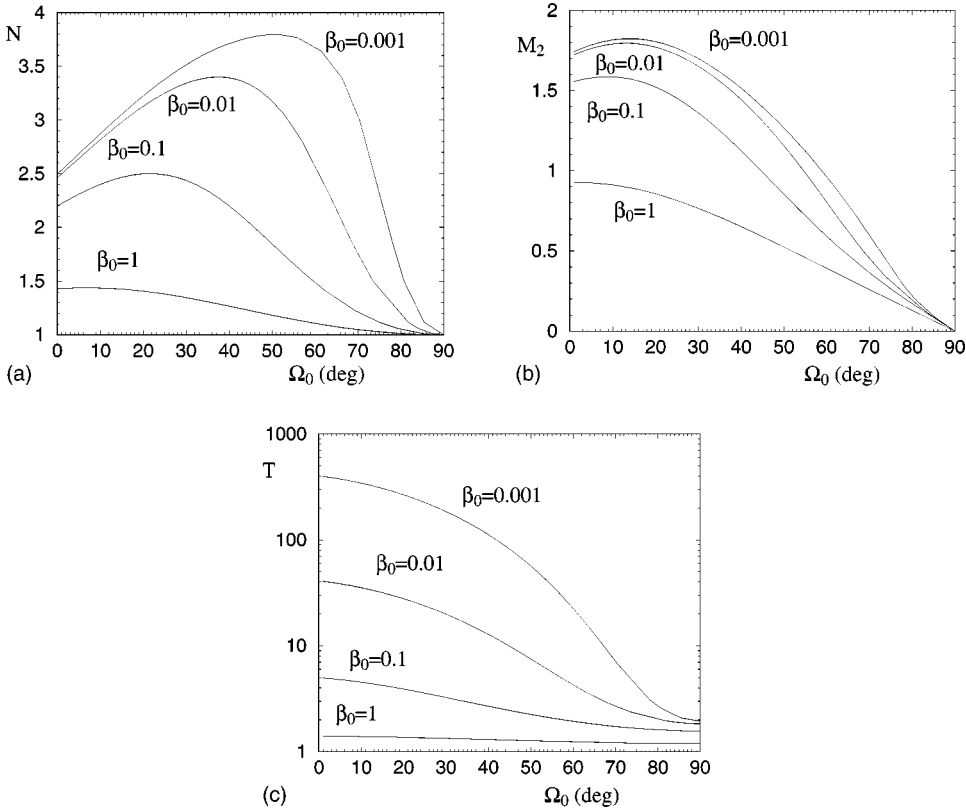The magnetosonic Mach number M_2 of the outflow is evaluated from

FIG. 2. Characteristics of the outflow in the Soward regime: (a) plasma compression $N=n_2/n_0$; (b) the magnetosonic Mach number M_2; (c) temperature jump $T=T_2/T_0$, shown as a function of Ω_0 for several values of the inflow plasma-to-magnetic pressure ratio β_0.

$$M_2 = \frac{v_2}{\sqrt{\dfrac{B_2^2}{\mu\rho_2}+\dfrac{5p_2}{3\rho_2}}} = \frac{V_r M_{A1r}\sqrt{N}}{\sqrt{\dfrac{B_r^2}{\cos^2\Omega_2}+\dfrac{5}{6}P\beta_{1r}}}. \quad (41)$$

The angle α between the inflow and the outflow velocity is related to other angles as

$$\alpha = \xi' - \phi - \vartheta. \quad (42)$$

The chosen input parameters are iteratively led in the numerical calculations to provide output results as functions of the inflow quantities β_0, Ω_0, M_{A00}, and α.

III. RESULTS

A. Basic dependences: The Soward regime

In Fig. 2 we first show the basic dependences of the density jump $N=n_2/n_1=n_2/n_0$, the outflow magnetosonic Mach number M_2, and the temperature jump $T=T_2/T_1=T_2/T_0$, on the angle Ω_0 to show the influence of the transversal magnetic field $\vec{B}_{z0}$. The results are obtained in the Soward regime applying several different values of the inflow plasma-to-magnetic pressure ratio β_0.

Figure 2(a) shows the generally stronger compression N for smaller β_0. Furthermore, at smaller β_0 the angle $\Omega_0(N_{max})$, at which the compression attains its maximum, is larger: it can be shown that for $\beta_0 \to 0$ the maximum of N asymptotically approaches $N \to 4$ at $\Omega_0 \to 90°$.

In Fig. 2(b) we show that the outflow Mach number M_2 is generally higher for smaller β_0, and strongly dependent on Ω_0. The interplay of Ω_0 and β_0 determines whether $M_2 > 1$, i.e., whether the outflowing jet is supermagnetosonic. It is possible to show that at $\Omega_0 = 0$ the outflow becomes sub-magnetosonic at $\beta_0 = 0.8$ [14–16].

Figure 2(c) shows that the plasma heating is stronger, i.e., the temperature jump T at SMS is higher for smaller β_0 (roughly governed by $T \propto \beta_0^{-1}$). The value of T decreases monotonously with increasing Ω_0: it drops to a half of the maximum value at $\Omega_0 \approx 30°$ [note the logarithmic scale on the y axis of Fig. 2(c)].

In the following subsection we explore deviations from the Soward regime, considering different speeds and directions of the inflow. Note that the reconnection rate in the fast reconnection regime can be up to $M_{A00} \approx 0.1$ [1], so we consider only the $M_{A00} = 0–0.1$ range. Furthermore, at $\Omega_0 = 45°$ the merging magnetic fields become perpendicular and the efficiency of the energy conversion drops significantly ([8], see also Figs. 2(b,c)). For this reason, in the following we focus on comparatively small angles Ω_0, in particular, $\Omega_0 = 0$ and $20°$.

B. Departure from the Soward regime

Let us first investigate how the characteristics of the outflowing jet depend on the reconnection rate M_{A00} [Eq. (44)]. The results are presented for three different angles of incidence, $\alpha = 30°$, $90°$, and $150°$, considering $\Omega_0 = 0$ (2D case) and $\Omega_0 = 20°$, with $\beta_0 = 0.01$ which is appropriate for describing the conditions in, e.g., solar flares [13].
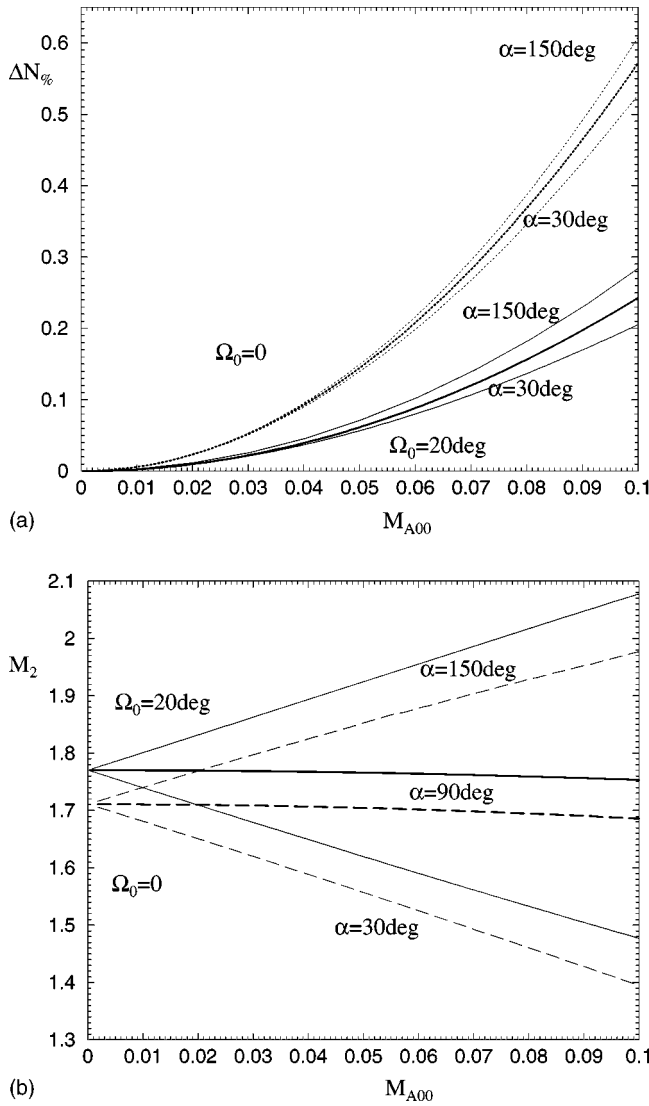
FIG. 4. Dependence of (a) relative difference $\Delta N_\%$ of the compression N and the Soward regime result N_S; (b) the outflow Mach number M_2, on the incidence angle α presented for the inflow Mach numbers $M_{A0}=0.01$ and 0.1 combined with $\Omega_0=0,20°$ at $\beta_0=0.01$.

FIG. 3. Dependence of (a) relative difference $\Delta N_\%$ of the compression N and the Soward regime value N_S; (b) the outflow Mach number M_2, on the reconnection rate M_{A00}. The results are presented for $\Omega_0=0$, 20°, and $\alpha=30°,90°,150°$ at $\beta_0=0.01$.

In Fig. 3(a) we show the departure of the compression $N=n_2/n_1=n_2/n_0$ from the value N_S in the Soward regime, utilizing $\Delta N_\%=100(N-N_S)/N_S$, since N is only weakly dependent on M_{A00}. The value of N increases with increasing reconnection rate, which is more pronounced for smaller angles Ω_0. When $M_{A00}\rightarrow0$, one finds that $N_\%\rightarrow0$, i.e., the values of N converge to N_S becoming independent of Ω_0, which is consistent with the Soward regime. A similarly weak dependence is found for the temperature jump $T=T_2/T_0$, where the value of T decreases with increasing M_{A00}.

Figure 3(a) reveals that the compression N depends slightly also on the incidence angle α: For a given Ω_0, the value of N is larger at larger α. Yet, the effect is an order of magnitude smaller than the influence of M_{A00}.

Figure 3(b) shows the dependence of the outflow magnetosonic Mach number on the reconnection rate $M_2(M_{A00})$. It is evident that M_2 depends significantly on the incidence
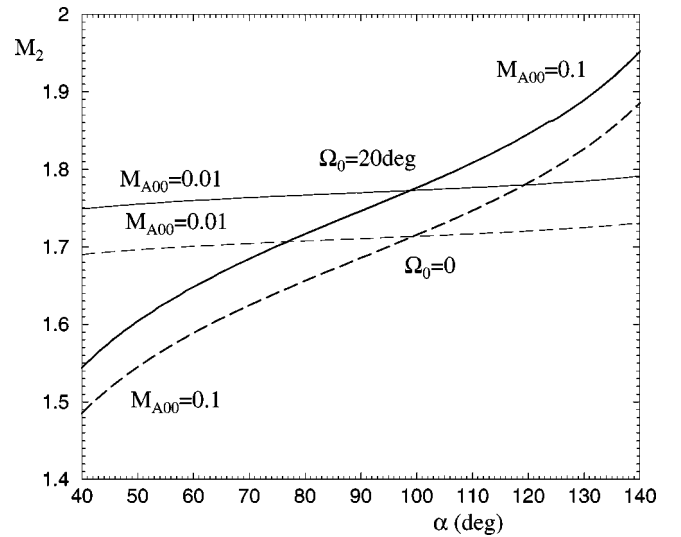
angle α, even more than on the angle Ω_0, however, only at comparatively large inclinations of the inflow. Around $\alpha=90°$ the outflow Mach number depends only weakly on M_{A00}, which indicates that the decrease/increase of M_2 for incidence angles smaller/larger than $\alpha=90°$ is primarily associated with the inflow velocity component parallel to the symmetry axis of the system. A slight decrease of $M_2(M_{A00})$ at $\alpha=90°$ is consistent with the increase of the compression $N(M_{A00})$ depicted in Fig. 3(a), since denser plasma can be convected out by a slower outflow (mass conservation).

Figure 4 illustrates the dependence of the outflow magnetosonic Mach number on the incidence angle $M_2(\alpha)$. We present the results for $M_{A00}=0.01$ and 0.1, again taking $\beta_0=0.01$ at $\Omega_0=0$ and 20°. The graph reveals a considerable change of M_2, but only for a comparatively large reconnection rate, while for low reconnection rates the Mach-Alfvén number M_2 remains close to the Soward regime results. The value of M_2 increases when the inflow has a component in the direction of the outflow, while it decreases for the inflow having a component in the direction opposite to the outflow.

We have examined this behavior quantitatively, and it has turned out that the net outflow speed is primarily a sum of two contributions: the "basic" outflow speed $v_2(\alpha=90°)$ and the tangential inflow component $v_{0\parallel}$. There is, however, a slight deviation (smaller than 0.1%) associated with the dependence of the compression N on the incidence angle α [Fig. 3(a)].

Finally, let us comment on a somewhat unexpected asymmetry present in Fig. 4—the curves $M_{A00}=0.1$ and $M_{A00}=0.01$ intersect at $\alpha\neq90°$, where the curves $M_{A00}=0.01$ closely resemble the values in the Soward regime ($M_2=1.71$ and 1.77 for $\Omega_0=0$ and 20°, respectively). The asymmetry is due to increasing compression N with increasing M_{A00}, which in turn reduces the value of M_2, i.e., shifts
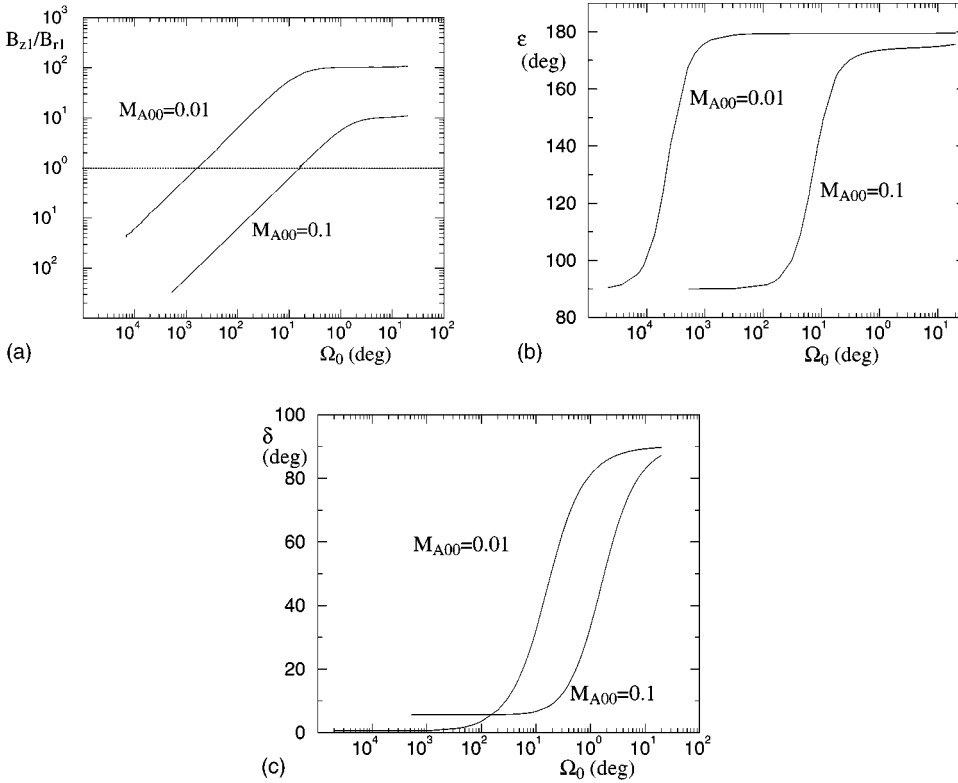
FIG. 5. Geometrical properties of the system in transition to 2D are explored: (a) Ω_1, (b) ε, (c) δ, shown as a function of Ω_0 for the value of the inflow plasma-to-magnetic pressure ratio $\beta_0 = 0.01$ and $\alpha = 90°$.

down the curve $M_2(\alpha)$ displacing the intersection with the Soward regime values towards larger values of α.

C. Geometrical properties of the system in the transition to 2D

The explicit solution of the complete set of equations presented in Sec. II provides an insight into the behavior of the geometry of the system in the transition from the $2\frac{1}{2}$D to the 2D regime ($\Omega_0 \to 0$, i.e., $B_{z0} \to 0$). As mentioned in Sec. II, it is assumed $B_{r1} \ll B_{z1}$ in the Soward regime. As a consequence, the angle ε remains close to 180° and δ close to 90° (i.e., $\vec{v}_1 \approx \vec{v}_2$ and $\vec{B}_1 \approx \vec{B}_2$, respectively). However, when $\Omega_0 \to 0$, i.e., in the transition to the 2-D geometry, this condition is obviously violated since $B_{z0} \to 0$ implies $B_{z1} \to 0$. Such a situation happens, e.g., in the so-called two-ribbon flares, where the initially sheared arcade of the magnetic field becomes stretched by eruption, naturally leading to the decrease of Ω_0, eventually coming to the $\Omega_0 \approx 0$ regime [10].

Let us examine some basic geometrical relationships in the intermediate region at the transition $\Omega_0 \to 0$. In Fig. 5(a) we show the behavior of the ratio of the transversal and the xy-plane components of the magnetic field in the intermediate region ($B_{z1}/B_{r1} = \tan \Omega_1$). The log-log presentation is used to show the relationship more clearly. At small angles, the slope of the log Ω_1(log Ω_0) dependence is very close to 1, i.e., the ratio B_{z1}/B_{r1} linearly decreases with decreasing B_{z0}/B_{r0}. At some point the Soward regime approximation $B_{z1} \gg B_{r1}$ is no longer satisfied [horizontal line drawn in Fig. 5(a) marks $B_{z1} = B_{r1}$].

In Fig. 5(b) and 5(c) the angles ε and δ are presented as functions of Ω_0, illustrating the behavior of the flow and the

magnetic field geometry (see Fig. 1) in the transition from the $2\frac{1}{2}$D to the 2D structure. The parameters used are $\beta_0 = 0.01$, $\alpha = 90°$, and $M_{A00} = 0.01$ and 0.1. Figure 5(b) and 5(c) reveal an extremely rapid change at small angles Ω_0 (note the logarithmic scale on the x axis). The transition from $\varepsilon \approx 180°$ to $\varepsilon \approx 90°$ happens in a very narrow range below Ω_0 at which $\tan \Omega_1 = B_{z1}/B_{r1} \approx 1$ [Fig. 5(a)], i.e., when the Soward regime breaks. Change of the direction of the xy-plane magnetic field component happens in a somewhat wider range of Ω_0.

IV. SUMMARY AND DISCUSSION

The presented analytical solution of the $2\frac{1}{2}$D symmetrical reconnection model provides an investigation of the dependence of the outflow characteristics on the inflow speed and the incidence angle. Furthermore, it enables tracing the geometrical changes in the intermediate region in the $B_{z0} \to 0$ regime, which cannot be properly described within the Soward model [8].

The results can be summarized as follows. (a) The outflow density ($N = n_2/n_0$) increases, and the temperature ($T = T_2/T_0$) decreases weakly with increasing inflow speed and incidence angle. The departure from the Soward regime does not exceed 1%.

(b) The outflow Mach number, i.e., the outflow velocity, depends significantly on the incidence angle and the effect increases with increasing reconnection rate.

(c) The flow/field geometry in the region between the rotational discontinuity and the slow-mode shock changes dramatically in the transition to 2D, e.g., at the reconnection rate

$M_{A00}=0.01$ the change $\varepsilon \approx 180° \rightarrow \varepsilon \approx 90°$ and $\delta \approx 90° \rightarrow \delta \approx 0$ happens within $\Omega_0 \lesssim 1°$.

Whereas the first item is of no practical interest really, the latter two might be of importance for the understanding of a range of phenomena. Most generally, the second item determines whether the outflow is submagnetosonic or supermagnetosonic. In the case of supermagnetosonic outflow, the quasiperpendicular fast-mode standing shock forms if the jet encounters an obstacle. Such a ''termination shock'' is detected in the so-called dynamical solar flares [15,17,18]. Since the outflow Mach number determines the termination shock amplitude it also governs the efficiency of the high-energy electron production in solar flares [19,20].

The situation where the incidence angle of the reconnection inflow significantly differs from $\alpha = 90°$ is met in the so-called ''solar coronal inflows'': Typically, a day after the coronal mass ejection, white-light coronagraph observations reveal numerous faint features moving towards the Sun at heights of 1–3 solar radii above the solar surface, with velocities of the order of 100 km s^{-1} [21,22]. These flows are interpreted as signatures of the gradual closing down of the magnetic flux dragged outwards by coronal mass ejections [22], i.e., as the downwards directed reconnection outflow. Very similar downwards directed flows are observed in soft x rays in the late stages of the long-duration dynamical flares, again being interpreted as the reconnection outflow [23,24]. Since the reconnection is located high in the corona in these events, it has to be considered that the process takes place in the outward streaming, solar wind environment. The solar wind flows at these heights exhibit velocities of the order of 100 km s^{-1} [25], whereas the observed perpendicular component of the reconnection inflows are of the order of 10 km s^{-1} [26]. This implies the incidence angle significantly smaller than 90°, and according to Fig. 4 one should expect considerably reduced velocity of the downwards reconnection outflow. Indeed, the described observed flows are much slower than the coronal Alfvén speed, which typically ranges between 500 and 1000 km s^{-1} [27].

The dependence of the reconnection outflow speed on the inflow incidence angle might be found also in the observations of the large dynamical flare [11]. Two flare-associated radio sources were spotted by the Nançay Multifrequency Radioheliograph at the sites where the standing fast-mode shocks in the reconnection outflows are expected. However, the upper one, located below the erupting filament was much stronger and more active. This indicates that the upper fast-mode shock is of larger amplitude than the lower one, implying also that the upwards directed reconnection outflow has larger Mach number than the downwards directed one, which is again consistent with the influence of the solar wind flow.

The characteristics of the system described in the last item imply that at small Ω_0 a very small perturbation of the transversal magnetic field component in the inflow region strongly influences the flow/field geometry in the intermediate region. Obviously, such a behavior might have consequences to the overall stability of the system. Consider a small perturbation of Ω_0 in the inflow region at some segment of RD: At this segment the flow/field directions will depart radically from those in the adjacent segments, which would presumably cause flow/field turbulence. Considering the supersonic outflow regime this could straightforwardly explain the stochastic and intermittent electron acceleration such as observed in solar flares [10,13].

APPENDIX

In the following the expressions abbreviated in Sec. II as $H, D, G, E,$ and F are written out:

$$H = \frac{\sin \omega}{\sin \delta'}, \tag{A1}$$

$$D = M_{A1r}^2 \frac{\sin \varepsilon}{\sin \delta} + \frac{B_r \cos \phi \left(\sin \delta - M_{A1r}^2 \dfrac{\sin^2 \varepsilon}{\sin \delta} \right)}{B_r \sin \varepsilon \cos \phi - V_r \sin \phi \sin \delta}, \tag{A2}$$

$$G = D \frac{B_r'^2 \sin \omega}{\sin \delta'} - \frac{V_r'^2 \sin \phi' (B_r'^2 \sin \omega \cos \omega - \sin \delta' \cos \delta')}{\sin \delta' (\sin \xi' \cos \xi' - V_r'^2 \sin \phi' \cos \phi')}, \tag{A3}$$

$$E = 2 M_{A1r}^2 (\sin^2 \varepsilon - N V_r^2 \sin^2 \phi) + \frac{1}{\cos^2 \Omega_1} - \frac{B_r^2}{\cos^2 \Omega_2}, \tag{A4}$$

$$\begin{aligned} F = &-\frac{1}{2} M_{A1r}^2 \left(\frac{\sin \varepsilon}{\cos^2 \Omega_V} - N V_r^3 \sin \phi \right) - \tan^2 \Omega_1 \sin \varepsilon \\ &+ B_r^2 V_r \tan^2 \Omega_2 \sin \phi - \cos^2 \delta \sin \varepsilon + B_r^2 V_r \sin^3 \phi \\ &+ \sin \delta \tan \Omega_1 \tan \Omega_V + \sin \delta \cos \delta \cos \varepsilon \\ &+ B_r^2 V_r \sin \phi \cos^2 \phi. \end{aligned} \tag{A5}$$

[1] E.R. Priest and T.G. Forbes, *Magnetic Reconnection* (Cambridge University Press, London, 2000).

[2] D. Biskamp, *Nonlinear Magnetohydrodynamics* (Cambridge University Press, Cambridge, UK, 1993).

[3] H.P. Furth, J. Killeen, and M.N. Rosenbluth, Phys. Fluids **6**, 459 (1963).

[4] M. Ugai, Phys. Fluids **30**, 2163 (1987).

[5] H.E. Petschek, in *AAS-NASA Symposium on Physics of Solar*

Flares, edited by W. N. Hess (NASA, Greenbelt, MA, 1964), pp. 425–439.

[6] H.E. Petschek and R.M. Thorne, Astrophys. J. **147**, 1157 (1967).

[7] A.M. Soward and E.R. Priest, J. Plasma Phys. **28**, 335 (1982).

[8] A.M. Soward, J. Plasma Phys. **28**, 415 (1982).

[9] P.J. Cargill and E.R. Priest, Sol. Phys. **76**, 357 (1982).

[10] B. Vršnak, Lect. Notes Phys. **612**, 28 (2003).

[11] B. Vršnak, K.-L. Klein, A. Warmuth, W. Otruba, and M. Skender, Sol. Phys. **214**, 325 (2003).

[12] M. Scholer, Lect. Notes Phys. **612**, 9 (2003).

[13] M.J. Aschwanden, Space Sci. Rev. **101**, 1 (2002).

[14] T.G. Forbes and J.M. Malherbe, Astrophys. J. Lett. **302**, L67 (1986).

[15] H. Aurass, B. Vršnak, and G. Mann, Astron. Astrophys. **384**, 273 (2002).

[16] M. Skender, B. Vršnak, and M. Martinis, in *Solar Variability: From Core to Outer Frontiers*, edited by A. Wilson (ESA, Noordwijk, 2002), pp. 757–760.

[17] M.J. Aschwanden, T. Kosugi, H.S. Hudson, M.J. Willsand, R.A. Schwartz, Astrophys. J. **470**, 1198 (1996).

[18] S. Masuda, T. Kosugi, S. Tsunetaand, and H. Hara, Adv. Space Res. **17**, 63 (1996).

[19] B.V. Somov and T. Kosugi, Astrophys. J. **485**, 859 (1997).

[20] S. Tsuneta and T. Naito, Astrophys. J. Lett. **495**, L67 (1998).

[21] T.S. Bastian, A.O. Benz, and D.E. Gary, Astron. Astrophys. **36**, 131 (1998).

[22] Y.M. Wang, N.R. Sheeley, Jr., R.A. Howard, and O.C. St. Cyr, Geophys. Res. Lett. **26**, 1203 (1999).

[23] D.E. McKenzie and H.S. Hudson, Astrophys. J. Lett. **519**, L93 (1999).

[24] D.E. McKenzie, Sol. Phys. **195**, 381 (2000).

[25] N.R. Sheeley, Jr. *et al.*, Astrophys. J. **484**, 472 (1997).

[26] T. Yokoyama, K. Akita, T. Morimoto, K. Inoue, and J. Newmark, Astrophys. J. Lett. **546**, L69 (2001).

[27] B. Vršnak *et al.*, Astron. Astrophys. **396**, 673 (2002).